Nanoscale

PAPER

View Article Online
View Journal | View Issue

Cite this: *Nanoscale*, 2024, **16**, 2945

Revealing microscopic dynamics: *in situ* liquid-phase TEM for live observations of soft materials and quantitative analysis *via* deep learning†

Yangyang Sun,[a] Xingyu Zhang, *[a] Rui Huang,[b] Dahai Yang,[b] Juyeong Kim, [c] Junhao Chen,[b] Edison Huixiang Ang, [d] Mufan Li,[e] Lin Li[f] and Xiaohui Song *[b]

In various domains spanning materials synthesis, chemical catalysis, life sciences, and energy materials, *in situ* transmission electron microscopy (TEM) methods exert a profound influence. These methodologies enable the real-time observation and manipulation of gas-phase and liquid-phase reactions at the nanoscale, facilitating the exploration of pivotal reaction mechanisms. Fundamental research areas like crystal nucleation, growth, etching, and self-assembly have greatly benefited from these techniques. Additionally, their applications extend across diverse fields such as catalysis, batteries, bioimaging, and drug delivery kinetics. However, the intricate nature of 'soft matter' presents a challenge due to the unique molecular properties and dynamic behavior of these substances that remain insufficiently understood. Investigating soft matter within *in situ* liquid-phase TEM settings demands further exploration and advancement compared to other research domains. This research harnesses the potential of *in situ* liquid-phase TEM technology while integrating deep learning methodologies to comprehensively analyze the quantitative aspects of soft matter dynamics. This study centers on diverse phenomena, encompassing surfactant molecule nucleation, block copolymer behavior, confinement-driven self-assembly, and drying processes. Furthermore, deep learning techniques are employed to precisely analyze Ostwald ripening and digestive ripening dynamics. The outcomes of this study not only deepen the understanding of soft matter at its fundamental level but also serve as a pivotal foundation for developing innovative functional materials and cutting-edge devices.

Received 6th September 2023,
Accepted 12th January 2024

DOI: 10.1039/d3nr04480g

rsc.li/nanoscale

1. Introduction

The advent of *in situ* liquid cell transmission electron microscopy (LP-TEM) has opened the door to real-time examination of liquid-phase phenomena. This includes the observation of processes like crystal nucleation and growth within solutions, the exploration of electrochemical reactions in energy materials, and the investigation of vital processes within living cells. Currently, there are three main approaches for characterizing samples in a liquid environment using transmission electron microscopy. One approach involves modifying the TEM setup to create a differential pumping vacuum system that allows a controlled amount of liquid near the sample stage.[1,2] Another approach employs low-vapor-pressure ionic liquids.[3] The third strategy encompasses enclosing the liquid within a closed chamber formed by two slender membrane windows. This design effectively shields the liquid from high vacuum surroundings of the electron microscope.[4] Among these approaches, the closed liquid cell technology is the most widely used due to its affordability and versatility. The choice of window material for the liquid cell needs to consider several factors, including mechanical strength, electron transparency, and impermeability to water or other liquids. Currently, window materials primarily include SiNx, graphene, and amorphous carbon. SiNx thin films serve as observation windows, and the liquid cell consists of two layers of silicon wafers. The thickness of SiNx thin films and the liquid layer

[a]*School of Mathematics, Statistics and Mechanics, Beijing University of Technology, Beijing 100124, China. E-mail: xingyu0711@bjut.edu.cn*
[b]*School of Materials Science and Engineering, Hefei University of Technology, Anhui Province230009, China. E-mail: xiaohuisong@hfut.edu.cn*
[c]*Department of Chemistry and Research Institute of Natural Sciences, Gyeongsang National University, Jinju 52828, South Korea*
[d]*Natural Sciences and Science Education, National Institute of Education, Nanyang Technological University, Singapore 637616, Singapore*
[e]*Institute of Physical Chemistry, the College of Chemistry and Molecular Engineering, Pecking University, Beijing, 100871, China*
[f]*Beijing Shunce Technology Co., Ltd, Beijing, 102629, China*
† Electronic supplementary information (ESI) available. See DOI: https://doi.org/10.1039/d3nr04480g

significantly affect imaging resolution. Reducing the thickness of SiNx while maintaining its mechanical strength is crucial for enhancing the performance of the liquid cell. Currently, SiNx thin film thickness can be reduced to around 10 nm, achieving atomic-level spatial resolution.[5,6] Graphene, being extremely thin and nearly transparent to electron beams, can effectively reduce or even eliminate electron scattering, enabling unprecedented high-resolution imaging. Moreover, graphene possesses high mechanical strength, good thermal and electrical conductivity, making it an ideal window material.

Taking advantage of its ability to achieve remarkable temporal and spatial precision while immersed in a liquid medium, liquid cell TEM technology offers a valuable means to explore diverse phenomena. These include the nucleation, growth,[7–9] and etching mechanisms of individual nanoparticles,[6,10–14] dynamic motion of nanoparticles in liquids,[15–18] electrochemical deposition and lithiation of electrode materials,[19–23] as well as imaging of biomaterials in liquid environments.[24–26] As *in situ* liquid-cell TEM techniques continue to mature and their application scope expands, there has also been a gradual emergence of studies focusing on soft matter.[27–30] Seamlessly integrating the contributions of various researchers, Park *et al.* employed real-time liquid-phase TEM to capture dynamic nanobubble behaviors, unveiling bulk and surface nanobubbles in the presence of soluble surfactants.[31] Lucas *et al.* employed *in situ* LP-TEM to witness the evolution of amphiphilic block copolymer micellar nanoparticles on the nanometer scale. Their observations unveiled growth mechanisms involving both unimer addition and particle collision-fusion.[32] Meanwhile, Liu *et al.* revealed amphiphilic block copolymers' self-assembly into core–shell micelles, encapsulating gold nanoparticles and featuring a hydrophobic core surrounded by a hydrophilic corona.[33] Alessandro Ianiro *et al.* highlighted liquid–liquid phase separation preceding amphiphilic self-assembly, where polymer-rich droplets act as precursors for evolving micelles and vesicles, influencing structural features and self-assembly kinetics.[34] Additionally, LP-TEM facilitated the induction and imaging of amphiphilic block copolymer self-assembly into spherical micelles *via* polymerization, while LP-TEM exposed bilayer formation through droplet or vesicle intermediates.[35] Moreover, the application of LP-TEM allowed the observation of nanoscale micelle nucleation and growth in the context of polymerization-induced self-assembly. This pointed towards the potential electron beam-induced radical generation from poly GMA-CTA, which initiates HPMA monomer polymerization within a water medium.[36] Diverse systems were investigated using graphene liquid cells, offering comprehensive insights from fabrication to successful sample identification, enabling precise examination of various materials and processes[37] Lastly, leveraging liquid-phase TEM and a U-Net neural network, Chen *et al.* demonstrated real-time imaging of colloidal nanoparticle systems, uncovering otherwise inaccessible nanoscale properties including anisotropic interactions, etching profiles, and kinetic assembly dynamics.[38]

Although similar research has been reported, several unresolved questions persist, such as the influence of surfactant molecules on liquid-phase environments, the kinetics of hollow structure dynamics in block copolymer vesicles, and confined self-assembly processes within *in situ* liquid phases. Addressing these requires further technological advancements, refined experimental design, and quantitative analysis through machine learning. This study employs GLC-TEM to investigate dynamic behaviors of four different subjects-nanobubbles, block copolymers, gold nanoparticles, and nano-sized sulfur particles-within electron beam-driven liquid environments. Utilizing deep learning, acquired data undergoes quantitative analysis, revealing unique growth or self-assembly patterns across the soft materials observed through *in situ* LC TEM. This methodology guarantees accurate examination while concurrently mitigating time and human resource expenditures. Our key findings include: (1) surfactant molecules stabilize bubbles, decreasing their mobility and merging rates; (2) surfactants enable controlled nanoparticle assembly within confined spaces; (3) block copolymer vesicles exhibit structural heterogeneity, self-hollowing to expand hollow volume, previously unreported; (4) accurate analysis of Ostwald ripening and digestive ripening during Au nanocrystal growth in the presence of organic surfactants.

Xiaohui Song

Dr Xiaohui Song is an associate professor of Materials Science and engineering at the Hefei University of Technology, China. He received his BS in Chemical Engineering from Wuhan University of Technology (China), and PhD in Chemistry from Nanyang Technological University (Singapore) in 2016. From 2017–2020, he continued his studies as a postdoctoral fellow at UIUC & UC Berkeley focusing on nanomaterials design and synthesis, especially the study of their structure–function relationships by using advanced electron microscopes and deep learning. He now leads a young and diverse group to build a toolbox by using advanced imaging & machine learning, which would be applied to nanomaterials design, and applications in energy storage.

2. Results and discussion

2.1 Surfactant molecules in deionized water (DI water)

Soft materials possess the capacity to react to variations in their surroundings. Considering that alterations transpire within the adjacent liquid during liquid-phase TEM imaging, comprehending, and managing this liquid environment is of paramount importance. Initially, our focus was on investigating the behavior of organic small molecules-surfactant

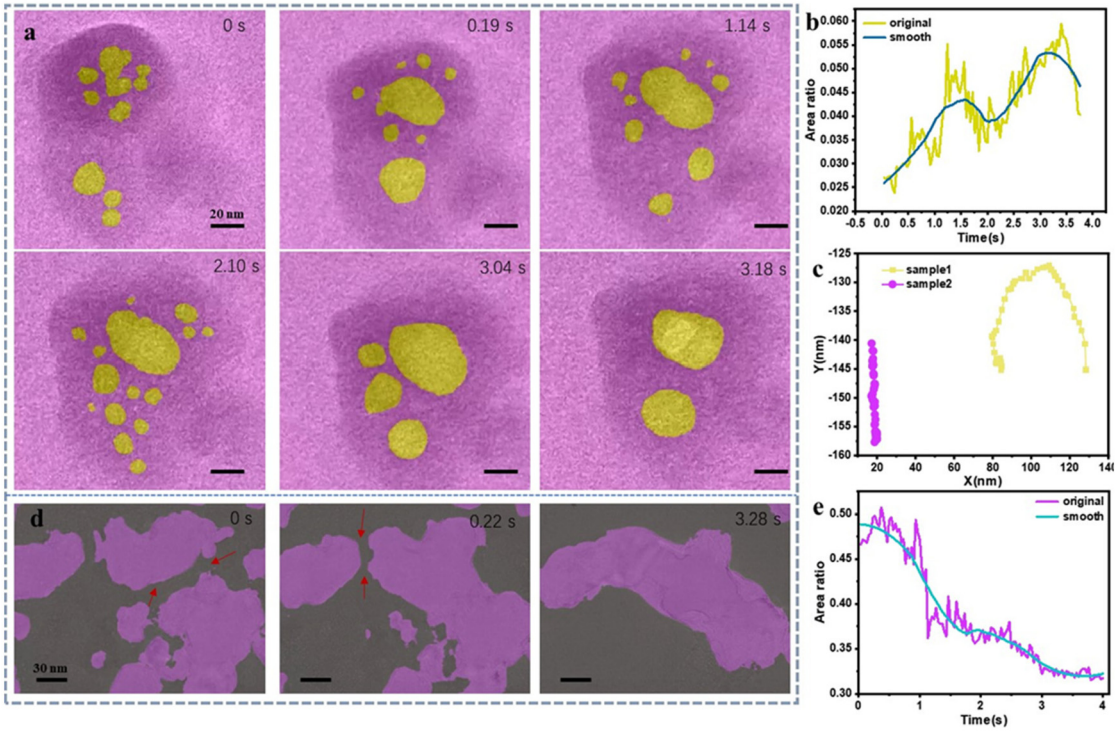

Fig. 1 *In situ* LCTEM experiments of DI water and Tween 80 aqueous solution. (a) Changes in the images of bubbles in the water under electron beam irradiation at different time. Graphs depicting the variation in bubble area (b) and (c) movement trajectories of the two types of bubbles mentioned above at the same time: the yellow curve represents the displacement of bubbles in water, and the purple bubbles represent the displacement of bubbles in a solution of surfactant molecules. (d) Changes in the bubble population over time upon addition of Tween 80, along with corresponding bubble area variations (e). Note: electron dose information is listed in ESI.† Notably, the reproducibility of the *in situ* TEM experiments is 4/5 based on our experience.

molecules-in aqueous solutions. We opted for a non-ionic surfactant called Tween 80 and created an aqueous solution with a concentration of 1.0×10^{-6} mM. *In situ* liquid-phase TEM experiments were carried out, utilizing both deionized water and solutions containing Tween 80. The analysis of *in situ* TEM data was conducted using the U-Net model, primarily leveraging the functionalities provided by the Dragonfly software. The primary objective was to analyze the impact of surfactant molecules on the formation of bubbles within the system (Fig. 1). Fig. 1a reveals that electron beam irradiation induces a multitude of rapidly moving bubbles in the aqueous solution. Similarly, to the phenomenon of Ostwald ripening, rapid bubble coalescence induces significant alterations in morphology and quantity (Movie 1†). This emphasizes the inherent kinetic instability of bubble formation within deionized water, attributed to the elevated surface energy at the interface between the bubble and water. The transformation in morphology, velocity, and the alteration in quantity together serve to highlight this aspect (Fig. 1b and c).

Significantly, we employed deep learning to process the video data (ESI discussion 1†), ensuring accurate image recognition and computation while enhancing efficiency, enhancing accuracy, and conserving human resources (Fig. S1–4†). Notably, In the analysis of the experimental video segment, a frame-by-frame manual annotation method was initially employed, necessitating approximately 3 hours per video for area change computations using software such as ImageJ. However, leveraging the capabilities of Dragonfly deep learning techniques significantly reduced the processing time to approximately 50 minutes per video, while concurrently augmenting accuracy. This improvement in efficiency and precision underscores the utility of employing advanced deep learning methodologies in our experimental analyses. This processing method was applied to all video analyses, with the accuracy of video data processing determined based on the loss function curve (Fig. S2b†).

In this scenario, the composition of the bubble would consist of DI water forming the liquid phase stabilized with the addition of Tween80 molecules, and the gas mixture of hydrogen and oxygen. The presence of Tween80 alters the characteristics of the bubble's liquid film, affecting its stability, surface tension, and interactions with the gas or vapor enclosed within the bubble. Hence, upon the introduction of surfactant molecules, a distinct shift in behavior is evident (Fig. 1d).

Firstly, there is a significant reduction in bubble movement speed. Secondly, bubble coalescence between neighboring bubbles occurs at a much slower rate (Movie 2†), even though the volume of bubbles in both experimental groups decreases (Fig. 1b and e). These observations indicate that the inclusion of surfactant molecules alters the bubble coalescence process.

The adsorption of surfactant molecules reduces the surface energy at the bubble-liquid interface, enhancing stability during the initial formation. This enhanced stability is manifested through the lowered movement speed and comparatively sluggish dynamics of bubble coalescence (Fig. 1c). Notably, In Fig. 1b and e, the smooth curve represents the curve fitted *via* moving average according to the original data, used to depict the trend of changes over time. The addition of Tween80 seems to enhance the stability of bubbles, making them less prone to rupture and better able to withstand higher surface tension. Simultaneously, incorporating Tween80 results in larger bubble sizes and a more diverse range of shapes, possibly due to an increased mass transfer between bubbles. However, we haven't analyzed the gas composition within the bubbles or the chemical reactions induced by beam irradiation due to limitations in our experimental conditions. These findings align closely with certain theoretical simulations,[39–41] leading to the conclusion that the addition of surfactants in deionized water effectively modulates bubble shape and restrains bubble deformation. This holds notable significance for controlling interfacial chemical reactions and mass transfer kinetics (ESI discussion 2†).

2.2 Surfactant molecules regulate self-assembly of gold nanoparticles in confinement

In order to further observe the impact of surfactant addition on the stability of the solution environment, we conducted the following experiment: 15-nanometer gold nanoparticles were dispersed in the two different types of liquids (deionized water, Tween 80 aqueous solution) whose surface zeta potential of Sodium citrate-stabilized gold nanoparticles is −29 mV, and −25 mV in Tween80 solution. The self-assembly characteristics of gold nanoparticles within the solution were monitored using *in situ* liquid-phase TEM. As depicted in Fig. 2a, the dynamic patterns of bubbles within a deionized water solution mirror the previously described scenario: rapid bubble motion and noteworthy alterations in morphology (Movie 3†). Moreover, due to rapid bubble coalescence, the internal gold nanoparticles aggregate more readily, forming clusters that further grow into larger-sized nanoparticles caused by particle fusion (Fig. 2b and Fig. S5a†). This phenomenon is also attributed to the high surface energy at the bubble-liquid interface, leading to the instability of bubbles and consequent aggregate growth. The area changes of bubble and encapsulated Au

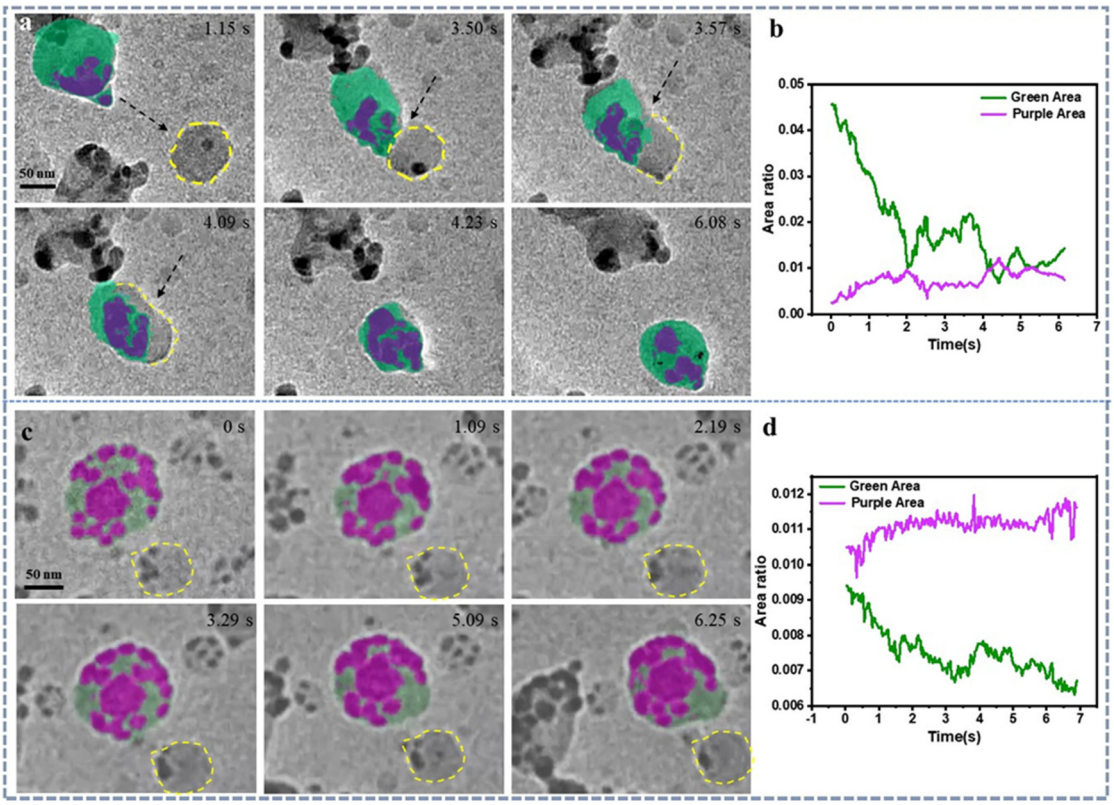

Fig. 2 *In situ* liquid-phase TEM observation of self-assembly behavior of gold nanoparticles in DI water and Tween 80 aqueous solution. (a) illustrates the temporal evolution of bubbles in the deionized water solution along with the changes in bubble area (green) and total area of gold nanoparticles (purple) over time (b). Notably, another bubble (yellow) did not merge with the marked one in the presence of surfactant. (c) shows the morphological changes of bubbles over time in the Tween 80 aqueous solution, along with the variation of bubble area (green) and total area of gold nanoparticles (purple) over time (d). Note: electron dose information is listed in ESI.† Notably, the reproducibility of the *in situ* TEM experiments is 2/7 based on our experience.

nanoparticles could be calculated accurately after 5 cycles training based on U-Net deep learning analysis (Fig. S5b†) and the convergence characteristics of the regression function curve supports this conclusion.

In contrast, the presence of surfactant molecules in the solution system significantly enhances bubble stability, resulting in reduced movement speed, relatively stable morphology, and size (Fig. 2c and d). Additionally, the internal gold nanoparticles maintain well-defined self-assembled ring like structures. Furthermore, real-time observations of nanobubble motion from both experimental groups indicate that the introduction of surfactant molecules leads to slower bubble movement (Movie 4†), suggesting increased stability due to the reduction in interfacial energy between gas and liquid (Fig. S6†). Whether it is changes in the morphology and volume of bubbles and gold nanoparticles, or variations in their movement speed, it can be observed that the addition of surfactant molecules is conducive to reducing surface energy, promoting bubble stability, and facilitating confined self-assembly based on the bubble's movement tracking (Fig. S7†). Conversely, the absence of surfactant molecules is favorable for the fusion and regrowth of gold nanoparticles. Our experimental findings indicate that the presence and varying concentration of surfactant molecules play a role in regulating nanoparticle self-assembly, particularly confinement-induced self-assembly. This outcome holds valuable insights for the study of self-assembly methodologies and the bottom-up design of nanomaterials by using gas–liquid–solid interface control *via* surfactant molecules. Notably, it is difficult to provide accurate value of liquid thickness. If we consider a relatively uniform spreading of 0.4 μL of water over a defined area between graphene layers, and assuming a consistent distribution, the liquid thickness might be in the range of tens of nanometers. This is a rough estimate and can vary depending on the specific characteristics of the graphene layers and their local interaction with water molecules in nanoscale. The movie quality of polymer layer looks good which means the liquid thickness might be in the range of tens of nanometers as we assumed.

2.3 Self-hollowing of block copolymers vesicles

Beyond exploring organic small molecules, our exploration extended to the application of *in situ* liquid-phase TEM technology in block copolymer systems. In contrast to surfactant solutions, these systems exhibit more intricate behaviors and have broader utility (drug delivery, biosensor, device). In this investigation, our focus was on the PS-*b*-PAA system. We formulated a solution with a monomer concentration of 8 mg mL^{-1} (DMF : water = 4.5 : 1, volume ratio). Employing *in situ* liquid-phase TEM imaging, we observed the emergence of vesicular structures (Fig. 3a). This observation aligns with numerous previously documented results: PSPAA

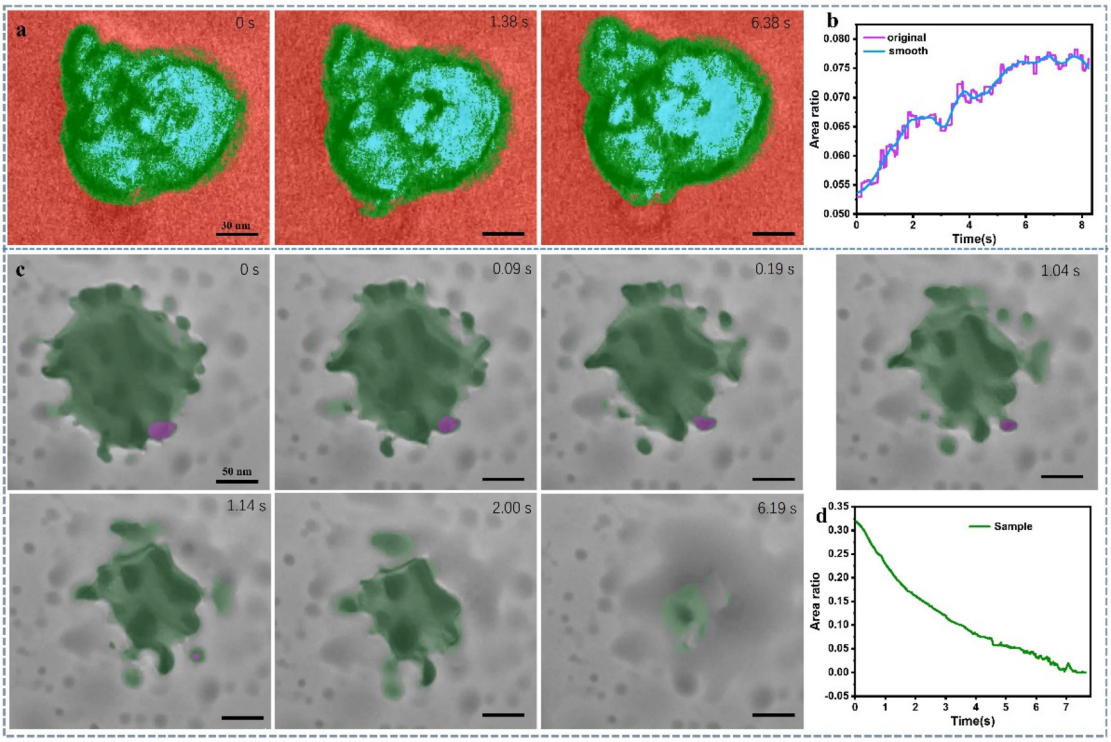

Fig. 3 Illustrates the real-time visualization of the self-hollowing dynamics within the block copolymer PS-*b*-PAA system using *in situ* liquid-phase TEM. (a) TEM images showing the temporal evolution of the 'self-hollowing' process within the assembled structure of PS-PAA vesicles. (b) Trend curve depicting the variation in the interior hollow structure area of PS-PAA vesicles over time. (c) Diagram illustrating the volatilization process of nano-sulfur under *in situ* liquid-phase TEM, along with the trend curve depicting its area change over time (d). Notably, the reproducibility of the *in situ* TEM experiments is 2/4 based on our experience.

serves as a nucleus for nanoparticle formation, subsequently leading to the assembly of cylindrical structures, and eventually evolving into vesicle configurations. Notably, when considering the electron beam effect on nano bubbles, two key factors come into play: electron-beam-induced radiolysis and heating effects. These factors can have varying implications when comparing the behavior of nano bubbles in deionized (DI) water and surface aqueous solutions. More discussions could be found in ESI (Discussion 3†). Based on our control experiments and literatures, we are inclined to believe that the self-hollowing phenomenon is a form of self-assembly induced by the heating effect of the electron beam in TEM. Notably, self-hollowing refers to the process within a fully formed PS-*b*-PAA particle where a transformation occurs from a solid to a hollow structure based our experimental finding.

Interestingly, during this experimental process, we discovered an "internal self-hollowing" phenomenon within the vesicles (Movie 5†). Concrete evidence of this process is the observable trend of increasing hollow structure area over time resolution (Fig. 3b and Fig. S8†). Notably, In Fig. 3b, the smooth curve represents the curve fitted *via* Moving Average according to the original data, used to depict the trend of changes over time. This self-hollowing hollowing process may be associated with internal polymer phase transitions, possibly induced by variations in the liquid environment, primarily pH changes in solution. Our *in situ* liquid-phase TEM experimentation serves as a favorable tool to study dynamic behaviors within polymer vesicles. Previous reports may not have extensively explored internal structural changes using this approach due to factors such as lower resolution and electron beam effects.[34,42,43]

Moreover, considering the sustained emphasis on energy materials in research (such as S NPs being used in Li–S battery), we sought to broaden the utilization of *in situ* liquid-phase TEM technology to investigate pertinent materials. Consequently, we devised experiments to monitor the evaporation behavior of nano-sized sulfur within the confines of *in situ* liquid-phase TEM conditions (depicted in Fig. 3c). Interestingly, contrary to conventional understanding, the solidification process of molten sulfur did not lead to the formation of a 'coffee ring' pattern. Instead, it exhibited rapid overall contraction and generated numerous mini liquid domains (Movie 6†). These regions subsequently underwent

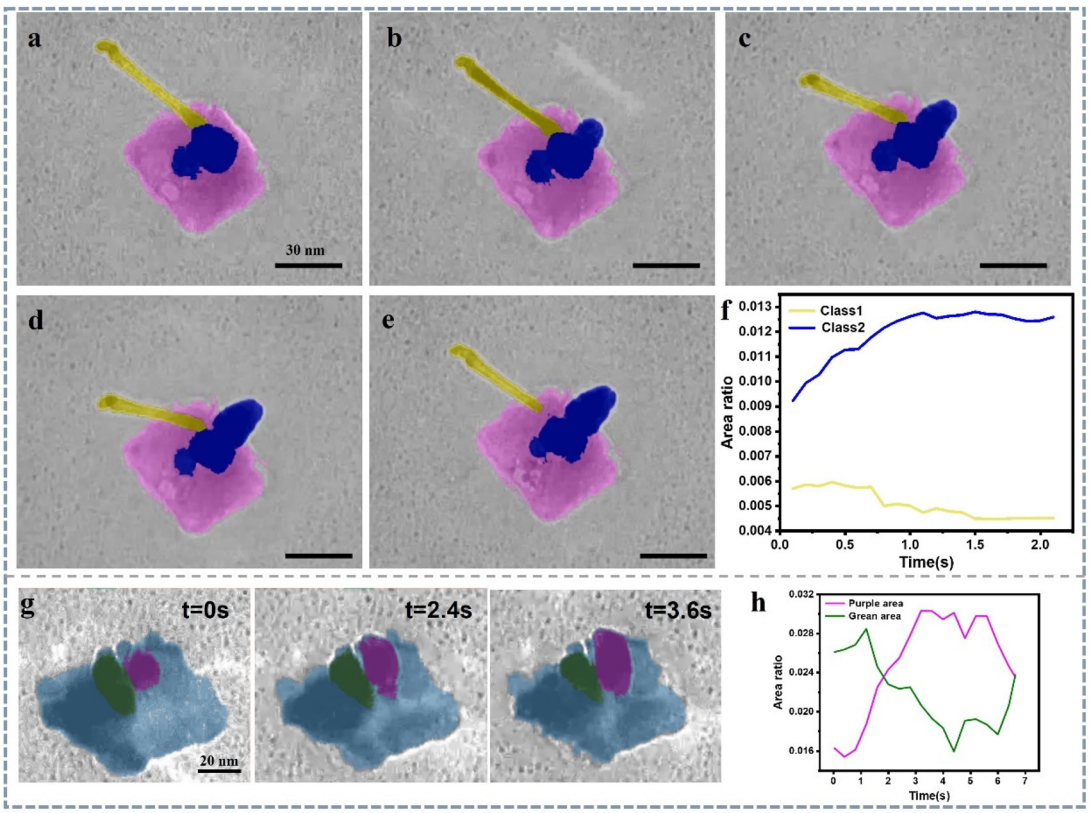

Fig. 4 *In situ* LCTEM observation of Ostwald ripening behavior during the growth process of gold nanowires. (a–e) Growth process of gold nanowires in a water solution with PVP as a ligand and surfactant, and ascorbic acid as a reducing agent. (f) Area variation curves over time for nanowire segments with different aspect ratios (yellow markers for high aspect ratio segments and blue markers for low aspect ratio segments) growing simultaneously. (g) Growth process (highlighted in yellow) of gold crystal in a water solution without PVP presence, and ascorbic acid as a reducing agent. (h) The area value trend curve during the Ostwald ripening process between the two Au nanocrystals. Notably, the reproducibility of the *in situ* TEM experiments is 4/4 based on our experience.

gradual sublimation, leaving no patterned traces but rather dispersed marks (Fig. 3d). The expeditious area contraction observed during the process underscores that molten sulfur's physical properties bear closer resemblance to liquids rather than colloids. This elucidates the absence of the 'coffee ring' phenomenon (Fig. S9 and 10†).

2.4 Ostwald ripening in the presence of surfactant

To investigate the growth process of nanomaterials in the presence of surfactants, we conducted the following experiment. We added chloroauric acid and ascorbic acid to a polyvinylpyrrolidone (PVP) aqueous solution with a molecular weight of 55 K. After thoroughly mixing the entire system, it was loaded for observation under *in situ* liquid-phase TEM. Fig. 4a–e illustrates a growth process similar to nanowires. Initially, the length of nanowires with smaller diameters (higher aspect ratio length: diameter = 8) decreases (yellow markers), followed by growth in the dimensions of regions with lower aspect ratios (blue markers), which is a typical Ostwald ripening phenomenon. Area calculations for the two regions (Fig. 4f) reveal distinct trends: the nanowire area in the yellow region decreases initially and stabilizes later, whereas the blue region exhibits a gradual increase in nanowire area before reaching stability (Fig. S11†). Intriguingly, both regions seem to possess pathways at their bottoms that potentially regulate mass transfer, resembling an intelligent self-regulation process (Movie 7†). The system appears to autonomously find an equilibrium structure based on its surroundings.

Precisely, based on our *in situ* experimental observations, this process exhibits a competitive mechanism between Ostwald ripening and digestive ripening, leading to crystalline growth occurring at different crystal interfaces at different times.[44,45] This phenomenon might be influenced by the localized concentration distribution of PVP molecules. Hence, we did a control experiment whose condition is the same as above without the present of PVP. The electron beam ON/OFF during TEM imaging is another control (Movie 8†). Through control experiments, we discovered that the absence of PVP primarily affects the morphology of the system. In this scenario, gold doesn't grow in the form of nanowires;

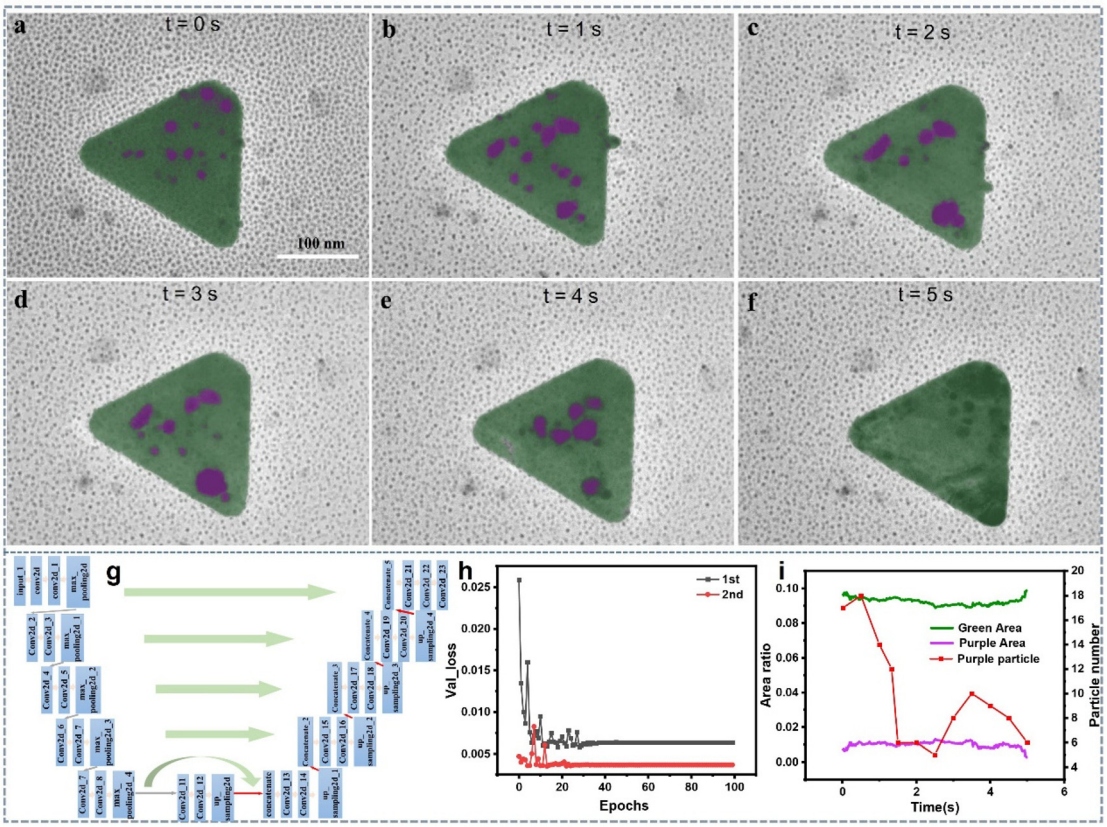

Fig. 5 *In situ* LCTEM observation of Ostwald ripening, nucleation, and encapsulation behavior during the growth process of gold on CTAB stabilized Au nanoplates. (a–f) Growth process of gold nanoparticle on CATB-Au plate in a water solution with CTAB as a ligand and surfactant (green: Au nanoplate; purple: Au nanoparticle). (g) Utilizing U-Net deep learning to process the Au nucleation dynamics on CTAB stabilized Au nanoplate. (h) The loss function curve processed through deep learning. (i) Area ratio variation curves over time for different morphology (green: Au nanoplate; purple: Au nanoparticle) growing simultaneously, and the Au nanoparticle number change-time curve (red). Notably, the reproducibility of the *in situ* TEM experiments is 2/5 based on our experience.

instead, it exhibits larger rod-like structures or irregular morphologies (Fig. 4g and Fig. S12†). Even under these experimental conditions, Ostwald ripening occurs (Fig. 4h). The electron beam ON/OFF directly dictates whether Ostwald ripening takes place or not.

2.5 Deep learning for quantitative analysis of gold nanoplate growth in organic ligand solutions

In the previous experiments, it can be observed that in the presence of non-ionic surfactant PVP, the growth mode of gold nanowires: first, they tend to grow into one-dimensional nanowires; second, there exists a competitive mechanism between Ostwald ripening and digestive ripening during the growth process.

Here, to compare the effects of different types of surfactants, we used another system: gold nanoplates solution synthesized with CTAB, with a concentration of 0.15 mM of the ionic surfactant CTAB. In this system, chloroauric acid was added as an oxidizing agent, and ascorbic acid as a reducing agent. The solution was then loaded into a graphene liquid cell for *in situ* observation. The experiment revealed that when no oxidizing or reducing agents were present, and only CTAB water solution was used, the gold nanoplates remained relatively stable without any etching phenomenon (Movie 9†). When chloroauric acid and ascorbic acid were added, redox reactions occurred in the solution, and the reduced gold atoms nucleated in the solution. Interestingly, the nucleation of gold atoms exhibited typical heterogeneous nucleation characteristics: many newly grown gold nanoparticles were found on the surface of the gold nanoplates (Fig. 5a–d), even there are some particles formed *via* self-nucleating in the solution. Moreover, competition between Ostwald ripening and digestive ripening was observed among these newly grown gold nanoparticles (Fig. 5a–e). Eventually, a significant deposition of gold atoms occurred on the surface of the gold nanoplates. This phenomenon, like what was observed in the PVP solution, demonstrates a common occurrence in the growth of gold nanostructures in liquid-phase environments.

In the data processing, we still employed deep learning techniques. In this study, we used both a 5-layer U-Net model (Fig. S13†) and a 6-layer U-Net model (Fig. S14†) for training. The accuracy of training can be assessed through the loss function. It was found that training the 6-layer U-Net model can more accurately identify and segment morphologies in video images. Through calculations, we could accurately analyze the area of different nanoparticles and their temporal changes (Fig. 5f–i). Additionally, by calculating the standard deviation, the quantitative analysis of the impact brought about by different image processing methods was achievable (Fig. 5f, g and Fig. S15†). The establishment of this model offers a new approach for precise structural analysis of complex nano-materials, while also saving time and human resources, thereby enhancing the efficiency of data processing.

3. Conclusion

Within this investigation, we delve into the nanoscale physical and chemical attributes of 'soft matter' through the amalgamation of *in situ* liquid-phase TEM technology and deep learning techniques. Our objective centers on the comprehensive characterization of 'soft matter' within its inherent liquid milieu, achieving a resolution on the nanometer scale. Firstly, we investigate small organic molecules, such as surfactant molecules, to understand their unique role in modulating the gas–liquid interface energy. This is crucial for the self-assembly and growth of nanomaterials, enabling responsive functionalities that evolve with changes in environmental factors like time, concentration, pH, and temperature. Examples include MOFs and super lattices. Secondly, we bridge interdisciplinary connections between different fields. This study encompasses materials science, electron microscopy,[43–45] as well as physics and machine learning.[46–49] Finally, our contribution extends to the progress of 'soft matter' exploration, specifically within the domain of organic soft matter. This field encompasses a multitude of valuable systems with tangible applications.

4. Methods and experimental

4.1. *In situ* liquid phase TEM imaging

Take two graphene-coated TEM grids and place them graphene side up on a glass slide. Using a small surgical scalpel blade, cut off the edge of one of the graphene-coated TEM grids, approximately 1/4 of the area of the grid.

The *in situ* liquid-phase TEM studies were conducted in a 120 kV TEM-1400 Flash TEM (JEOL Ltd, Tokyo, Japan) equipped with a Gatan camera (Gatan Inc., Pleasanton, CA, USA). The *in situ* image series were acquired at a rate of 2 frames per second and an incident electron flux of $<0.1\ e^{-}\ Å^{-2}\ s^{-1}$.

4.2. Liquid solution preparation

4.2.1. DI water. The water solution utilized in this experiment is deionized water sourced from the Millipore Milli-Q® Integral 10 Water Purification System. The remaining experimental steps and details are the same as described above: approximately 0.4 μL of water droplet is deposited onto the graphene film, and then assembled into a liquid graphene pocket, serving as the sample for *in situ* liquid phase TEM experiments.

4.2.2. Tween80 aqueous solution. First, prepare a water solution of surfactant: the non-ionic surfactant Tween80 is used in this experiment, with a concentration of 5.0×10^{-7} mol L^{-1}, and deionized water as the solvent. After preparing the solution, allow it to stand undisturbed to ensure uniformity and prevent the formation of any bubbles.

4.2.3. Au NP aqueous solution. Sodium citrate-stabilized gold nanoparticles, with a size of 15 nm, are dispersed in deionized water solution at a concentration of 0.005 mg ml^{-1}.

This solution is utilized for *in situ* liquid-phase TEM experiments. The detailed steps are described in ESI.†

Notably, details experimental information, imaging procedure, and data analysis *via* deep learning could be found in ESI Note 2 from ESI.†

Data availability

The data are available from corresponding authors based on reasonable requirement. All details of the experiments can be found in ESI.†

Author contributions

X. S. and X. Z. conceived the idea and directed the writing. X. S., Y. S., D. Y., J. K., and R. H., designed the *in situ* TEM and TEM imaging experiments. X. S., Y. S., X. Z., E. H. A., and M. L. designed the Au nanoparticle synthesis and materials normal characterizations. X. S., X. Z., R. H., L. L., and Y. S., analyzed the *in situ* TEM movies. X. S., J. C., and X. Z., design the *ex situ* experiments and normal sample preparation & characterization. All authors commented on the manuscript and contributed to the discussion of the writing.

Conflicts of interest

The authors declare no competing financial interest.

Acknowledgements

Dr Song thanks the financial support of Start-up Grant from Hefei University of Technology (grant number: 13020-03712021026). Dr Kim thanks the financial support from National Research Foundation of Korea (2022R1A4A1022252) and KBSI NFEC (2019R1A6C1010042). Dr. Zhang thanks Beijing Postdoctoral Grant (2022-ZZ-068) and Chaoyang District Postdoctoral Grant (2022ZZ-18).

References

1 T. W. Hansen, J. B. Wagner and R. E. Dunin-Borkowski, *Mater. Sci. Technol.*, 2010, **26**, 1338–1344.
2 P. L. Gai, *Microsc. Microanal.*, 2002, **8**, 21–28.
3 J. Y. Huang, L. Zhong, C. M. Wang, J. P. Sullivan, W. Xu, L. Q. Zhang, S. X. Mao, N. S. Hudak, X. H. Liu and A. Subramanian, *Science*, 2010, **330**, 1515–1520.
4 M. Williamson, R. Tromp, P. Vereecken, R. Hull and F. Ross, *Nat. Mater.*, 2003, **2**, 532–536.
5 H. Zheng, R. K. Smith, Y.-W. Jun, C. Kisielowski, U. Dahmen and A. P. Alivisatos, *Science*, 2009, **324**, 1309–1312.
6 H.-G. Liao, D. Zherebetskyy, H. Xin, C. Czarnik, P. Ercius, H. Elmlund, M. Pan, L.-W. Wang and H. Zheng, *Science*, 2014, **345**, 916–919.
7 Z. Wang, C. Liu and Q. Chen, *J. Cryst. Growth*, 2023, **601**, 126955.
8 N. D. Loh, S. Sen, M. Bosman, S. F. Tan, J. Zhong, C. A. Nijhuis, P. Král, P. Matsudaira and U. Mirsaidov, *Nat. Chem.*, 2017, **9**, 77–82.
9 M. H. Nielsen, S. Aloni and J. J. De Yoreo, *Science*, 2014, **345**, 1158–1162.
10 F. Liu, X. Lu, C. Zhu, Z. Bian, X. Song, J. Sun, B. Zhang, J. Weng, A. Subramanian and X. Tong, *ACS Nano*, 2023, **17**(13), 12603–12615.
11 Q. Chang, D. Yang, X. Zhang, Z. Ou, J. Kim, T. Liang, J. Chen, S. Cheng, L. Cheng and B. Ge, *Nanoscale*, 2023, **15**, 13718–13727.
12 Y. Jiang, G. Zhu, F. Lin, H. Zhang, C. Jin, J. Yuan, D. Yang and Z. Zhang, *Nano Lett.*, 2014, **14**, 3761–3765.
13 S. W. Chee and M. G. Burke, *Liquid Cell Electron Microscopy*, 2017, p. 258.
14 J. M. Yuk, J. Park, P. Ercius, K. Kim, D. J. Hellebusch, M. F. Crommie, J. Y. Lee, A. Zettl and A. P. Alivisatos, *Science*, 2012, **336**, 61–64.
15 X. Fu, B. Chen, J. Tang, M. T. Hassan and A. H. Zewail, *Science*, 2017, **355**, 494–498.
16 U. Anand, J. Lu, D. Loh, Z. Aabdin and U. Mirsaidov, *Nano Lett.*, 2016, **16**, 786–790.
17 W. C. Lee, B. H. Kim, S. Choi, S. Takeuchi and J. Park, *J. Phys. Chem. Lett.*, 2017, **8**, 647–654.
18 S. Zhou, J. Li, J. Lu, H. Liu, J.-Y. Kim, A. Kim, L. Yao, C. Liu, C. Qian and Z. D. Hood, *Nature*, 2022, **612**, 259–265.
19 D. Yang, Y. X. A. Ng, K. Zhang, Q. Chang, J. Chen, T. Liang, S. Cheng, Y. Sun, W. Shen and E. H. Ang, *ACS Appl. Mater. Interfaces*, 2023, **15**, 20583–20602.
20 Q. Chang, Y. X. Angel Ng, D. Yang, J. Chen, T. Liang, S. Chen, X. Zhang, Z. Ou, J. Kim and E. H. Ang, *ACS Mater. Lett.*, 2023, **5**, 1506–1526.
21 E. R. White, S. B. Singer, V. Augustyn, W. A. Hubbard, M. Mecklenburg, B. Dunn and B. C. Regan, *ACS Nano*, 2012, **6**, 6308–6317.
22 A. J. Leenheer, K. L. Jungjohann, K. R. Zavadil and C. T. Harris, *ACS Nano*, 2016, **10**, 5670–5678.
23 S.-Y. Lee, J. Shangguan, J. Alvarado, S. Betzler, S. J. Harris, M. M. Doeff and H. Zheng, *Energy Environ. Sci.*, 2020, **13**, 1832–1842.
24 J. Park, H. Park, P. Ercius, A. F. Pegoraro, C. Xu, J. W. Kim, S. H. Han and D. A. Weitz, *Nano Lett.*, 2015, **15**, 4737–4744.
25 Q. Chen, J. M. Smith, J. Park, K. Kim, D. Ho, H. I. Rasool, A. Zettl and A. P. Alivisatos, *Nano Lett.*, 2013, **13**, 4556–4561.
26 C. Wang, Q. Qiao, T. Shokuhfar and R. F. Klie, *Adv. Mater.*, 2014, **26**, 3410–3414.
27 Z. Ou, X. Song, W. Huang, X. Jiang, S. Qu, Q. Wang, P. V. Braun, J. S. Moore, X. Li and Q. Chen, *ACS Appl. Mater. Interfaces*, 2018, **10**, 40990–40995.

28 Z. Lyu, L. Yao, W. Chen, F. C. Kalutantirige and Q. Chen, *Chem. Rev.*, 2023, **123**, 4051–4145.
29 Z. Ou, C. Liu, L. Yao and Q. Chen, *Acc. Mater. Res.*, 2020, **1**, 41–52.
30 Z. Ou, A. Kim, W. Huang, P. V. Braun, X. Li and Q. Chen, *Curr. Opin. Solid State Mater. Sci.*, 2019, **23**, 41–49.
31 Y. Bae, S. Kang, B. H. Kim, K. Lim, S. Jeon, S. Shim, W. C. Lee and J. Park, *Engineering*, 2021, **7**, 630–635.
32 L. R. Parent, E. Bakalis, A. Ramírez-Hernández, J. K. Kammeyer, C. Park, J. De Pablo, F. Zerbetto, J. P. Patterson and N. C. Gianneschi, *J. Am. Chem. Soc.*, 2017, **139**, 17140–17151.
33 C. Liu, L. Yao, H. Wang, Z. R. Phua, X. Song and H. Chen, *Small*, 2014, **10**(7), 1332–1340.
34 A. Ianiro, H. Wu, M. M. van Rijt, M. P. Vena, A. D. Keizer, A. C. C. Esteves, R. Tuinier, H. Friedrich, N. A. Sommerdijk and J. P. Patterson, *Nat. Chem.*, 2019, **11**, 320–328.
35 A. Rizvi, J. T. Mulvey and J. P. Patterson, *Nano Lett.*, 2021, **21**, 10325–10332.
36 V. Jabbari, A. H. Phakatkar, A. Amiri, A. Ghorbani and R. Shahbazian-Yassar, *Macromolecules*, 2023, **56**, 3171–3182.
37 H. Wang, Z. Xu, S. Mao and S. Granick, *ACS Nano*, 2022, **16**, 18526–18537.
38 L. Yao, Z. Ou, B. Luo, C. Xu and Q. Chen, *ACS Cent. Sci.*, 2020, **6**, 1421–1430.
39 S. A. Hewage and J. N. Meegoda, *Colloids Surf., A*, 2022, **650**, 129565.
40 G. Nagayama, T. Tsuruta and P. Cheng, *Int. J. Heat Mass Transfer*, 2006, **49**, 4437–4443.
41 H. Peng, G. R. Birkett and A. V. Nguyen, *Adv. Colloid Interface Sci.*, 2015, **222**, 573–580.
42 T. J. Woehl, T. Moser, J. E. Evans and F. M. Ross, *MRS Bull.*, 2020, **45**, 746–753.
43 P. M. Pelz, *et al.*, *ACS Nano*, 2021, **16**, 588–596.
44 X. Song, *et al.*, *ACS Mater. Lett.*, 2020, **3**, 171–178.
45 X. Song, *et al.*, *ACS Appl. Mater. Interfaces*, 2019, **11**, 8517–8526.
46 Z. Lyu, *et al.*, *Chem. Rev.*, 2023, **123**, 4051–4145.
47 B. Han, *et al.*, *Adv. Mater.*, 2022, **34**, 2108252.
48 A. A. Melo, *et al.*, *Nat. Commun.*, 2022, **13**, 7641.
49 Y. Tian, R. Liang, A. Kumar, P. Szwedziak and J. H. Viles, *Chem. Sci.*, 2021, **12**, 6896–6907.